# Experimental and Computational Phase Boundary Mapping of $Co_4Sn_6Te_6$

| | |
|---|---|
| Journal: | *Journal of Materials Chemistry A* |
| Manuscript ID | TA-ART-08-2018-007539.R1 |
| Article Type: | Paper |
| Date Submitted by the Author: | 28-Sep-2018 |
| Complete List of Authors: | Crawford, Caitlin; Colorado School of Mines, Material Science<br>Ortiz, Brenden; Colorado School of Mines, Material Science<br>Gorai, Prashun; Colorado School of Mines, Metallurgical and Materials Engineering; National Renewable Energy Laboratory,<br>Stevanovic, Vladan; Colorado School of Mines, Metallurgical and Materials Engineering; National Renewable Energy Laboratory,<br>Toberer, Eric; Colorado School of Mines, Physics; National Renewable Energy Laboratory, |
| | |

Journal Name

ARTICLE TYPE

Cite this: DOI: 10.1039/xxxxxxxxxx

Received Date
Accepted Date

DOI: 10.1039/xxxxxxxxxx

www.rsc.org/journalname

# Experimental and Computational Phase Boundary Mapping of $Co_4Sn_6Te_6$ †

Caitlin M. Crawford,[a] Brenden R. Ortiz,[a], Prashun Gorai,[b,c] Vladan Stevanovic,[b,c] and Eric S. Toberer[a,c]*

Binary $Co_4Sb_{12}$ skutterudite (also known as $CoSb_3$) has been extensively studied, however, its mixed-anion counterparts remain largely unexplored in terms of their phase stability and thermoelectric properties. In the search for complex anionic analogs to the binary skutterudite, we begin by investigating the $Co_4Sb_{12}$ - $Co_4Sn_6Te_6$ pseudo-binary phase diagram. We observe no quaternary skutterudite phases and as such, focus our investigations on the ternary $Co_4Sn_6Te_6$ via experimental phase boundary mapping, transport measurements, and first-principles calculations. Phase boundary mapping using traditional bulk syntheses reveal that the $Co_4Sn_6Te_6$ exhibits electronic properties ranging from degenerate $p$-type to intrinsic behavior. Under Sn-rich conditions, Hall measurements indicate degenerate $p$-type carrier concentrations and high hole mobility. The acceptor defect $Sn_{Te}$ and donor defects $Te_{Sn}$ and $Co_i$ are the predominant defects and rationally correspond to regions of high Sn, Te, and Co, respectively. Consideration of the defect energetics indicates $p$-type extrinsic doping is plausible, however $Sn_{Te}$ is likely a killer defect that limits $n$-type dopability. We find that the hole carrier concentration in $Co_4Sn_6Te_6$ can be further optimized by extrinsic $p$-type doping under Sn-rich growth conditions.

## 1 Introduction

Skutterudites are one of the highest performing classes of thermoelectric materials, with figure of merit ($zT$) well in excess of unity.[1–5] Despite the rich compositional landscape, much of this work has been focused on variations of the binary skutterudite, $Co_4Sb_{12}$.[6] Here we refer to this skutterudite as $\Box Co_4Sb_{12}$ for clarity, where $\Box$ refers to an interstitial void. This void space within $Co_4Sb_{12}$ has provided a path to lower the lattice thermal conductivity through the insertion of point defects.[7–13]. Traditionally, $n$-type $Co_4Sb_{12}$-based skutterudites have achieved high $zT$ due to their conduction band degeneracy, high intrinsic mobility, and incorporation of phonon scattering sources to lower the natively high lattice thermal conductivity; yielding $zT$ values up to 1.4[5]. In contrast, $p$-type $Co_4Sb_{12}$ based skutterudites have shown less attractive electronic properties; peaks $zT$ values of 0.2 - 0.6 have been achieved through reduction of lattice thermal conductivity.[8,14–17] Prior computational efforts have suggested that the valence band electronic structure can be radically altered through altering the anion chemistry.[18]

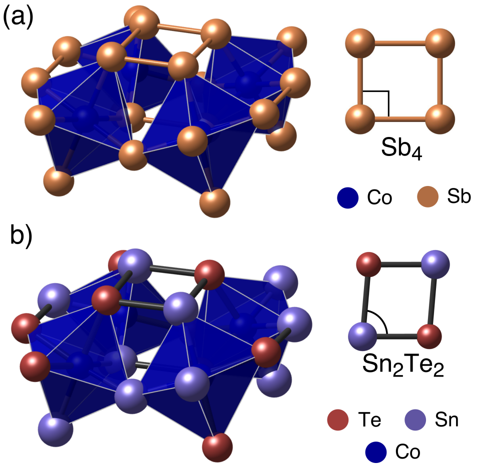

**Fig. 1** (a) Half-cell view of the cubic $Co_4Sb_{12}$ skutterudite structure. The homo-nuclear $Sb_4$ rings are rectangular with an aspect ratio of $\sim$0.95 (b) Half-cell view of the mixed-anion $Co_4Sn_6Te_6$ skutterudite. The replacement of Sn and Te on the Sb sites causes the octahedra to distort and the symmetry of the system to decrease to rhombohedral. The anion rings shift from rectangular to rhomboidal to account for the variable anion species ($Sn_2Te_2$).[19]

---

[a] Physics, Colorado School of Mines, Golden, CO USA.
[b] Metallurgical and Materials Engineering, Colorado School of Mines, Golden, CO USA.
[c] National Renewable Energy Laboratory, Golden, CO, USA.
* Email: etoberer@mines.edu

† Electronic Supplementary Information (ESI) available.

Mixed-anion skutterudites can be formed when the pnictogen (*Pn*) anion is replaced with equal parts tetrel and chalcogen atoms. Generally, this unfilled skutterudite remains isoelectronic to its binary analog and takes the form of $M_4X_6Y_6$ (where M = Co, Rh, Ir; X= Ge, Sn; Y= S, Se, Te).[20,21] In this work, we specifically focus on the $Co_4Sn_6Te_6$ ternary as it is chemically the closest to the $Co_4Sb_{12}$ binary skutterudite. The substitution of antimony with equal parts group IV and VI elements causes the overall symmetry of the system to reduce from cubic to rhombohedral ($Im\bar{3}$ space group to $R\bar{3}$).[22] The global distortion is a result of the replacement of the homo-nuclear $Sb_4$ rectangular rings to hetero-nuclear $Sn_2Te_2$ rhomboidal rings (Fig. 1). It has also been theorized that the group IV anion has a stronger bond with the transition metal than that of the group VI anion, aiding in the reduction of symmetry.[23–26]

To date, most work on the mixed-anion skutterudites has been on undoped samples or motivated primarily by theory.[10,20–22,27–36] For reference, *p*-type $Co_4Sb_{12}$ has a band gap of 0.25 eV, and a single Kane-like valence band at Γ with a light effective mass. This band dominates the upper 0.5 eV of the valence electronic structure; below this a range of high effective mass bands can be found. Various calculated electronic band diagrams for $Co_4Sn_6Te_6$ suggest the splitting of the anion site increases the band gap to ∼0.5 eV and increases the effective mass.[18,35] The valence band structure changes significantly, as the low-lying bands move to within 200 meV of the band edge. Further alterations to the electronic structure can be made by the introduction of interstitial rattlers, $\square Co_4Sn_6Te_6$ ($\square$ = Ca), which are expected to increase the band gap as well.[37]

Experimental studies on $Co_4Sn_6Te_6$ yield much higher resistivity than the binary analog. Room temperature resistivity values for $Co_4Sn_6Te_6$ range from 2000-5000 mΩ-cm while $Co_4Sb_{12}$ ranges from roughly 33-100 mΩ-cm.[8,11,35,38] Prior Hall measurements are inconclusive as the bipolar effects are potentially quite strong in such undoped materials.[35] Extrinsic doping studies have not been reported to date in $Co_4Sn_6Te_6$; *n*-type doping has been achieved in the analogous $Co_4Ge_6Se_6$ via interstitial Ce and Yb.[39] In addition, the ternary skutterudite natively has a lower lattice thermal conductivity (3 W/m K)[35] compared to the binary analog (6-8 W/m K)[11].

To date, the majority of the experimental $Co_4Sn_6Te_6$ literature show varying levels of impurity phases, suggesting a potentially narrow phase stability region.[27,28,30,31,34–36] The presence of impurities coupled with the intrinsic transport behavior in prior samples suggests compensating defects. One strategy to understand the defects and their impact in $Co_4Sn_6Te_6$ is phase boundary mapping; this is a synthetic procedure to pin a sample to a specific set of elemental chemical potentials during equilibration. In a ternary system, this implies that excess constituents are added until the desired phase exists in equilibrium with two impurity phases. By pinning the elemental chemical potentials, the intrinsic defect concentrations are thus fixed.[40,41] Multiple studies for filled binary skutterudites, $R_xCo_4Sb_{12}$ (R= In, Ga, Ce, Yb), have utilized this technique to increase the overall filling fraction, control the carrier concentration, and resolve discrepancies in the literature.[3,42–44] For example, in the study of $Ce_xCo_4Sb_{12}$, the three phase region $Co_4Sb_{12}$-$Ce_xCo_4Sb_{12}$-$CoSb_2$ turned out to be the relevant invariant point for maximizing filling fraction. Regardless of the quantities of $Co_4Sb_{12}$ or $CoSb_2$, the $Ce_xCo_4Sb_{12}$ is invariant.[3] Intermediate, single-phase compositions are in fact ambiguous in terms of their elemental chemical potentials and thus ambiguous in terms of their defect concentrations and synthetic repeatability. Thus, mapping the (multiple) compositional invariant points provides fundamental extrema and a deeper understanding of the single-phase region. To date, phase boundary mapping has been unexplored for $Co_4Sn_6Te_6$.

In this work, we pave the path to understanding the phase stability and thermoelectric properties of the $Co_4Sn_6Te_6$ skutterudite and its relationship to $Co_4Sb_{12}$. We begin by investigating the range of anion ring stoichiometry achievable in the Co-Sb-Sn-Te phase space. We then focus on the phase boundary mapping of the mixed-anion skutterudite by investigating the ternary phase space surrounding $Co_4Sn_6Te_6$ through a combination of experiment and theory. We intentionally synthesized multi-component samples to yield a $Co_4Sn_6Te_6$ matrix with compositions at phase boundary invariant points (i.e. phase boundary mapping). High temperature electronic transport measurements were aquired for samples with compositions connected to the invariant points. These results were then mapped to calculations of native defects for invariant point compositions. Depending on composition, we find that $Co_4Sn_6Te_6$ can be synthesized as either an intrinsic semiconductor (e.g. Te-rich) or a degenerate *p*-type semimetal (e.g. Sn-rich). Our defect calculations agree with experiment, indicating that extrinsic degenerate *p*-type doping should be possible, owing to the absence of competiting intrinsic defects. However, achieving *n*-type transport will require specific synthetic conditions to avoid compensating defects.

## 2 Methods

### 2.1 Experimental

All samples were produced by combining stoichiometric ratios of cobalt powder (Alfa 99.998%), tin shot (Alfa 99.99+%), antimony shot (Alfa 99.999%), and tellurium lump (Alfa 99.999+%) in an argon glovebox. Sn/Te rich samples were formed via a SnTe precursor; the SnTe was formed via melt in an evacuated quartz ampoule at 850 °C. Mixtures were then milled in tungsten carbide SPEX vials for two hours in one hour increments under an argon atmosphere with a ball-to-mass ratio of approximately 3:1 and a ball diameter of 1/2 inch. The resulting powders were then annealed in evacuated fused-silica ampoules with a ramp rate of 5 °C/min to 625 °C, held at temperature for 24 hours, and allowed to cool to room temperature. Annealed powders were then ground and sieved through a 106 micron mesh adhering to ASME Standard E-11. For compositions where transport measurements were taken, the annealed powders were then loaded into graphite dies and hot pressed under a uniaxial load of 80 MPa at 600 °C for roughly 6 hours under dynamic vacuum. Densities were measured via Archimedes method with deionized water as the working fluid.

Powder X-ray Diffraction (PXRD) data were obtained at room

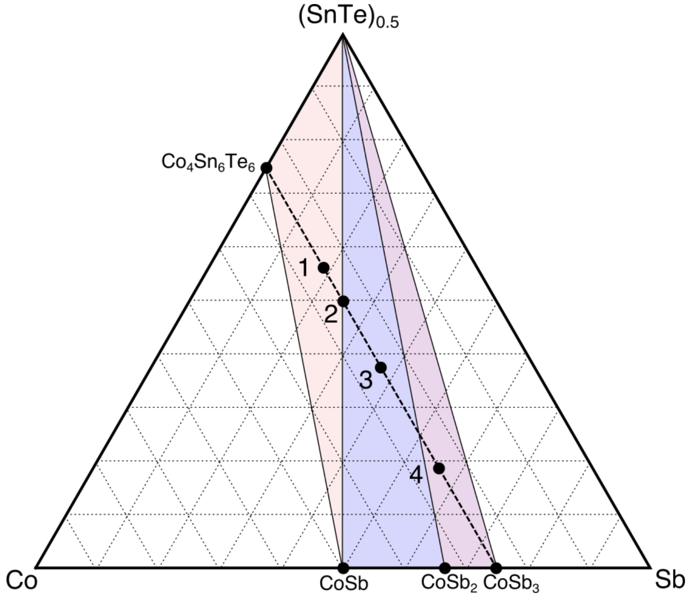

**Fig. 2** Co - Sb - $(SnTe)_{0.5}$ Experimental ternary phase diagram: Samples 1-4 are experimentally synthesized and lie along the $Co_4Sb_{12}$ - $Co_4Sn_6Te_6$ pseudo-binary highlighted by the black dashed line. The nominal compositions of samples 1,3 and 4 were chosen based on their potential anion ring ratios. The XRD in Fig. ES1 allows us to define our Alkemade lines shown here by the encompassed colored triangles. We see no presence of a quaternary skutterudite in this phase space.

temperature via a Bruker D2 Phaser diffractometer in a $\theta$ - $2\theta$ configuration with a divergence slit of 1 mm and a Cu K$\alpha$ tube radiation source. One sample was sent to the 11-BM beamline at the Advanced Photon Source of Argonne National Laboratory. Diffraction patterns were analyzed using Rietveld refinement *via* the TOPAS Academic software package.[45] A FEI Quanta 600i environmental scanning electron microscope (ESEM) was utilized for imaging and determining sample composition.

The Seebeck coefficient $S$ was determined via the quasi-steady slope method on a custom apparatus under high vacuum ( $<$ $10^6$ Torr) up to 300 °C. Both the Hall effect and electrical resistivity measurements were measured on a custom apparatus using the Van der Pauw method. Nichrome-wire pressure-assisted contacts were employed. The measurements were conducted under vacuum up to 300 °C.[46]

### 2.2 Computational

The formation energetics of native point defects in $Co_4Sn_6Te_6$ are calculated with first-principles using density functional theory (DFT) in the standard supercell approach[47]. The formation energy ($\Delta H_{D,q}$) of a point defect $D$ in charge state $q$ is calculated as:

$$\Delta H_{D,q} = (E_{D,q} - E_H) + \sum_i n_i \mu_i + qE_F + E_{corr} \qquad (1)$$

where $E_{D,q}$ is the total energy of the supercell containing defect $D$ in charge state $q$ and $E_H$ is the energy of the host supercell. The chemical potential of element $i$ is denoted by $\mu_i$ and $n_i$ is the number of atoms of element $i$ added ($n_i$<0) or removed ($n_i$>0) from the supercell. $E_F$ is the Fermi energy. The supercell approach to calculating defect energetics suffers from finite size artificats. These corrections are grouped into the $E_{corr}$ term and briefly discussed in the following paragraphs. A more detailed description of these corrections can be found elsewhere[47]. $E_{corr}$ comprises all the finite-size corrections within the supercell approach. The following corrections are included in $E_{corr}$: (1) image charge correction for charge defects, (2) potential alignment correction for charged defects, (3) band filling correction for shallow defects. The calculation setup and analyses are performed using a software package for automation of point defect calculations.[48]

To calculate the total energies of the supercells, the generalized gradient approximation (GGA) of Perdew-Burke-Ernzerhof (PBE)[49] is utilized in the projector augmented wave (PAW) formalism as implemented in the VASP software[50]. An on-site correction of 3 eV in the form of Hubbard U in a rotationally invariant form[51] is applied to the $d$ orbitals of Co. The position of the ions in the defect supercells are relaxed following the procedure used in Ref. 52. The total energies of the relaxed defect supercells containing 96 atoms are calculated with a plane-wave energy cutoff of 340 eV and a $\Gamma$-centered Monkhorst pack k-point grid to sample the Brillouin zone.

The elemental chemical potential $\mu_i$ is expressed relative to the reference elemental phase as $\mu_i = \mu_i^0 + \Delta\mu_i$, where $\mu_i^0$ is the chemical potential of the reference phase (under standard conditions) and $\Delta\mu_i$ is the deviation from $\mu_i = \mu_i^0$. $\Delta\mu_i = 0$ corresponds to $i$-rich growth conditions. The reference elemental chemical potentials are fitted to a set of measured heat of formation at 300K, using a procedure similar to that described in Ref. 52. The fitted reference elemental chemical potentials are more accurate than simply using the 0K DFT-calculated total energies as demonstrated in Refs. 41,52. For a given compound, the bounds on $\Delta\mu_i$ is set by the region of phase stability.

Defect energetics of vacancies ($V_{Co}$, $V_{Sn}$, $V_{Te}$), antisites ($Sn_{Te}$, $Te_{Sn}$), and interstitials ($Co_i$, $Te_i$) in charge states $q =$ -3, -2, -1, 0, 1, 2, and 3 are calculated. Vacancies and antisites derived from all unique Wyckoff positions in the crystal structure are considered in the calculations. The most likely sites for interstitials are identified by Voronoi tessellation as implemented in the software package[48]. The position of the equilibrium Fermi energy at a given temperature is calculated self-consistently by establishing the charge neutrality condition. Calculated valence band and conduction band density-of-states (DOS) effective masses of 0.170 eV and 4.514 eV, respectively, were used for calculations of hole and electron concentrations.

## 3 Experimental Results

To investigate the opportunity-space for mixed anion skutterudites, we begin by considering the Co - Sb - $(SnTe)_{0.5}$ pseudo-ternary by synthesis of samples along the $Co_4Sb_{12}$ - $Co_4Sn_6Te_6$ pseudo-binary line. From there, we specifically consider the ternary skutterudite, $Co_4Sn_6Te_6$, through experimental phase boundary mapping, transport measurements, and calculation of the defect energetics. First principles defect calculations provide intrinsic defect levels and highlight growth conditions needed for successful extrinsic doping.

### 3.1 $Co_4Sb_{12}$ - $Co_4Sn_6Te_6$ Pseudo-Binary

Samples formed with compositions $Co_4Sb_{12x}Sn_{6(1-x)}Te_{6(1-x)}$ (where x = 1/4, 1/3, 1/2, 3/4) were formed to investigate if Sn, Sb, and Te could simultaneously be incorporated onto the skutterudite anion rings. These compositions can be seen on the Co - Sb - $(SnTe)_{0.5}$ pseudo-ternary in Fig. 2. Synthesis conditions were initially optimized for $Co_4Sn_6Te_6$, with nominally phase pure samples characterized by lab PXRD and SEM (ES2). Refinement of the X-ray diffraction patterns for samples across the pseudo-binary line (ES3) does not suggest the presence of a new phase. For example, sample one separates into three phases (CoSb, SnTe, and $Co_4Sn_6Te_6$) which is consistent with the suggested Alkemade lines defined in Figure 2. These X-ray results allows us to map out the Alkemade lines relevant for this ternary space of interest, yielding the phase diagram presented in Fig. 2. From these experimental results, we conclude that the mixing of Sn, Sb, and Te on the ring sites is energetically unfavorable when compared to segregation into a mixture of binary and ternary end members. This suggested isothermal phase diagram is largely consistent with DFT phase stability calculations performed in this work (Supplemental ES4). For both theory and experiment, SnTe is found to be an end-member of all available Alkemade triangles in the pseudo-ternary. This suggests SnTe is a deep thermodynamic well. However, theory does not pick up the stability of $CoSb_2$, as it is slightly above (0.039 meV/atom) the convex hull between CoSb and $CoSb_3$.

Thus, despite the known solubility of Sn and Te on the $CoSb_3$ anionic sublattice, these results find that the simultaneous mixing of all three anions does not result in a skutterudite-like phase. This could be due to the bonding angles and therefore distortion of the ring network by the introduction of variable anions. In the Sn-Te rings, the acute Te-Sn-Te bond angles are compensated by obtuse bond angles in Sn-Te-Sn, yielding a near-rhombus geometry. In contrast, forming a $SnSb_2Te$ ring may induce significant bond strain as the bond angles are not complementary. Due to the lack of quaternary skutterudite, we focus the remainder of this work on understanding the ternary phase space of the $Co_4Sn_6Te_6$ skutterudite.

### 3.2 $Co_4Sn_6Te_6$ Ternary Phase Space

With this understanding of the Sn-Sb-Te ring chemistry and the strong driving force for segregation into $Co_4Sn_6Te_6$, we focus our attention to the ternary Co-Sn-Te phase space. These efforts allow the identification of invariant points for phase boundary mapping.

We begin by experimentally investigating the Co-Sn-Te phase space via traditional bulk synthesis. Using the methods described above, we synthesized various samples in the Co-Sn-Te ternary to map out the Alkemade lines of the system. This gives us a clearer understanding of the neighboring phases surrounding the $Co_4Sn_6Te_6$ single-phase region. As seen in Fig. 3, the samples produced (as indicated by the grey and blue points on the ternary) define the competing phases via X-ray diffraction analysis. For example, $Co_9Sn_4Te_7$ (blue point) diffraction spectra can be deconvoluted into the combined patterns of CoSn, $Co_{1-x}Te$, and $Co_4Sn_6Te_6$ from the Inorganic Crystallographic Structure Database (ICSD). Let Figure 3 serve as a guide to the Co-Sn-Te phase space, however note that the widths of each region were not explored in this work. Although prior literature has been thin on investigating the phases neighboring the mixed-anion skutterudite, the prior work performed shows evidence of secondary phases of SnTe and possibly $Co_{1-x}Te$.

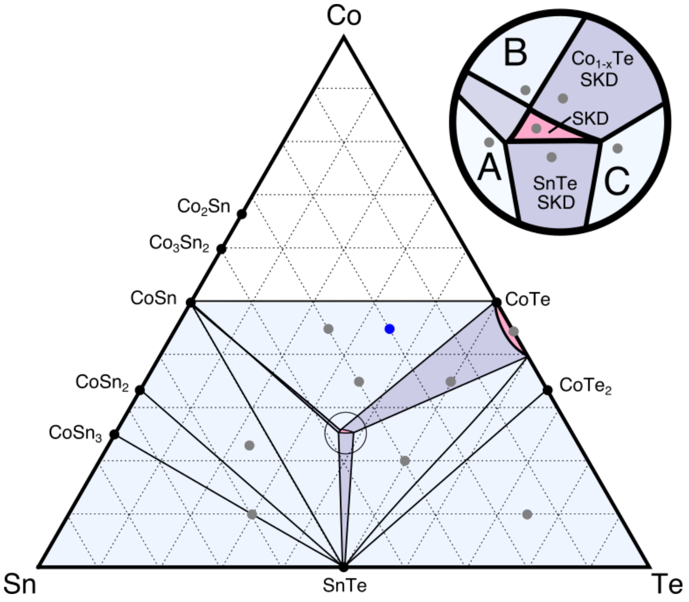

**Fig. 3** A proposed Co-Sn-Te ternary phase diagram at 600°C was generated experimentally using diffraction data (gray and blue points). The blue point was analyzed *via* synchrotron XRD (ES5). One-, two-, and three- phase regions are pink, purple, and blue, respectively. Inset shows phases surrounding the ternary Co-Sn-Te skutterudite, which are the focus of our phase boundary mapping study. We omit Co-rich samples due to lack of phase equilibria with skutterudite.

Blue and purple regions on the diagram indicate three-phase and two-phase regions, respectively. Pink regions on the phase diagram indicate single-phase regions with some solubility observed. We find that CoTe is an off stoichiometric compound, $Co_{1-x}Te$, with a region of solubility along the Co-Te binary. Intentionally synthesizing a sample in the two-phase region connecting $Co_{1-x}Te$ and $Co_4Sn_6Te_6$ only indicates the presence of these two phases. We note that again SnTe appears to be a dominating phase in this phase space as evidenced by the number of Alkemade lines connecting it to neighboring phases. Of the eight possible Alkemade lines that could connect to SnTe, six compounds form pseudo-binaries with SnTe (minimum required is one). As a result, we can expect that the skutterudite may have a narrow stability region due to its competing neighboring phases.

With a coarse understanding of the phase boundaries, we turn to a second set of samples that are presented in Figure 4. These samples are closer to the skutterudite composition and exist within two- and three- phase regions neighboring the skutterudite phase. We produced samples in the three-phase regions (A, B, and C in inset of Fig. 3) to determine the compostional invariant points of the single-phase region for $Co_4Sn_6Te_6$. In addition,

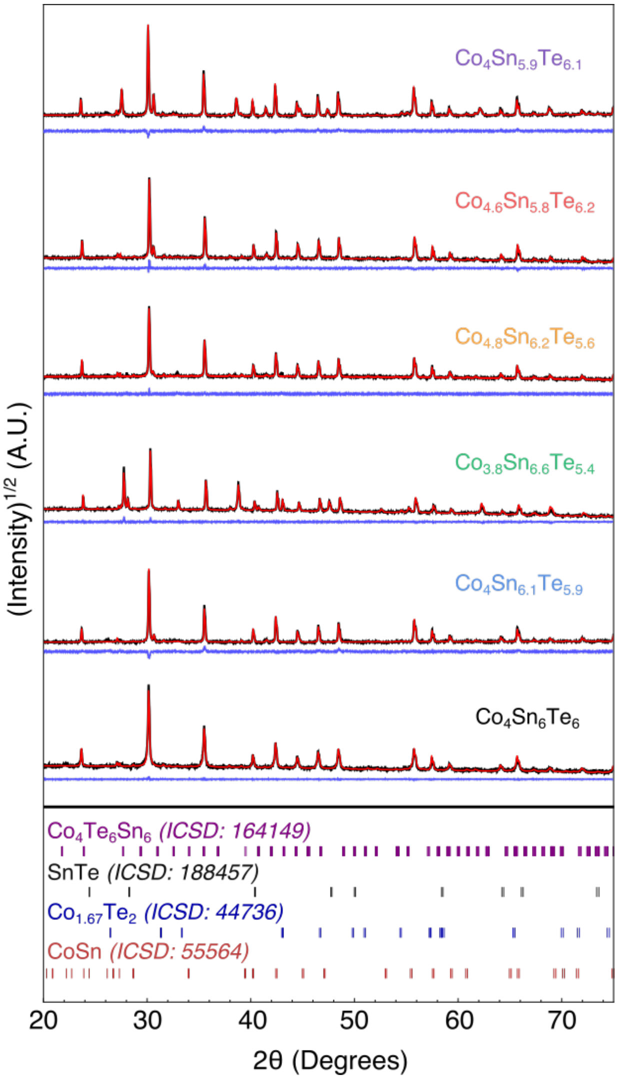

**Fig. 4** TOPAS refined X-ray diffraction data for samples seen in Fig. 3 inset. Nominal compositions have been colored to correspond to their transport data below. ICSD reference patterns are provided as stick plots. Experimental data, TOPAS fit and the difference profiles are shown (black, red, and blue respectively). Refinement values can be found in supplemental (ES6). Intensity has been plotted on a square root scale to intensify the secondary peaks.

we made two samples in the two-phase regions. Efforts to make the sample in the two-phase region connecting $Co_4Sn_6Te_6$ and CoSn yielded trace SnTe or $Co_{1-x}Te$, suggesting it has a narrow stability region. The X-ray diffraction data in Figure 4 for these samples is consistent with the ternary in Figure 3, verifying our suggested Alkemade lines. This set of samples allows us to begin investigating $Co_4Sn_6Te_6$ through phase boundary mapping by determining the transport behavior of the invariant points.

### 3.3 Transport

Electronic measurements were performed for this second set of samples neighboring the single-phase skutterudite region as seen in Figure 5. Only the sample in region A shows degenerate electronic behavior (1.5 mΩ-cm at 300 K), with all other samples exhibiting room temperature resistivity values in excess of 100 mΩ-cm. We observe promising mobility for this sample as well, with a room-temperature value of roughly 110 $cm^2$/V-s and a carrier concentration of $3 \times 10^{19}$ $cm^{-3}$. High temperature measurement of the resistivity and Hall coefficient reveal a gradual linear decay in mobility with increasing temperature and the carrier concentration remains essentially constant. As such, it appears the sample in region A, of composition $Co_{3.8}Sn_{6.6}Te_{5.4}$, is a degenerate semiconductor with high electronic mobility likely limited by phonon scattering. Figure 6 reveals that the Seebeck coefficient rises monotonically with increasing temperature. This, coupled with the temperature-independent carrier concentration, supports the claim that the sample is a degenerate semiconductor. Assuming a parabolic band model and single carrier type, we calculate the density of states effective mass of the valence band edge from this sample's Seebeck data to be $0.10\,m_e$ at 300 °C. However, the calculated effective mass increased with temperature, consistent with the Seebeck coefficient not linearly extrapolating to 0 uV/K at 0 K. These values are consistent with the calculated effective mass of $0.17\,m_e$ from DFT. The observed mobility is also exceptionally consistent with prior studies of $Co_4Sb_{12}$ at similar carrier concentrations (with Br and Sn as a dopant). As the effective masses are also similar, this suggests the relaxation times in these two compounds are comparable.[53]

All other compositions yield large resistivity values, indicating these compositions may be intrinsic. Due to the intrinsic transport, a detailed analysis of the bipolar Hall and Seebeck coefficient transport would required further knowledge of the band structure and scattering rates for both charge carrier types. As such, further analysis is precluded. For example, the single band model for Hall mobility significantly underestimates the actual carrier mobility when minority carriers are present in a significant concentration. Bipolar effects are particularly pernicious in this material because of the massive difference in effective masses of the conduction and valence band edges, $4.5\,m_e$ and $0.17\,m_e$, respectively. These intrinsic findings are consistent with the limited electronic measurements reported for this system. Zevalkink *et. al.* observed high resistivity and mixed conduction behavior with the mixed-anion skutterudite (with trace SnTe).[35]

From these transport data, we see that preparing $Co_4Sn_6Te_6$ in equilibrium with trace secondary phases via phase boundary mapping yields variable electronic properties without extrinsic doping. These data suggest the potential for *p*-type doping the mixed-anion skutterudite if grown in Sn-rich conditions, similar to the sample produced in region A. Te-rich conditions lead to intrinsic properties, as seen above from all non-A samples and those samples reported in literature. From these experimental results, it is not yet clear if Te-rich conditions favor dopability.

## 4 Computational Results

Native point defects play a critical role in determining properties of semiconductors including their dopability *i.e.* the achievable free carrier concentrations of a specific type (electrons or holes). The dopability of a semiconductor is largely determined by the formation energetics of native defects, which among other factors

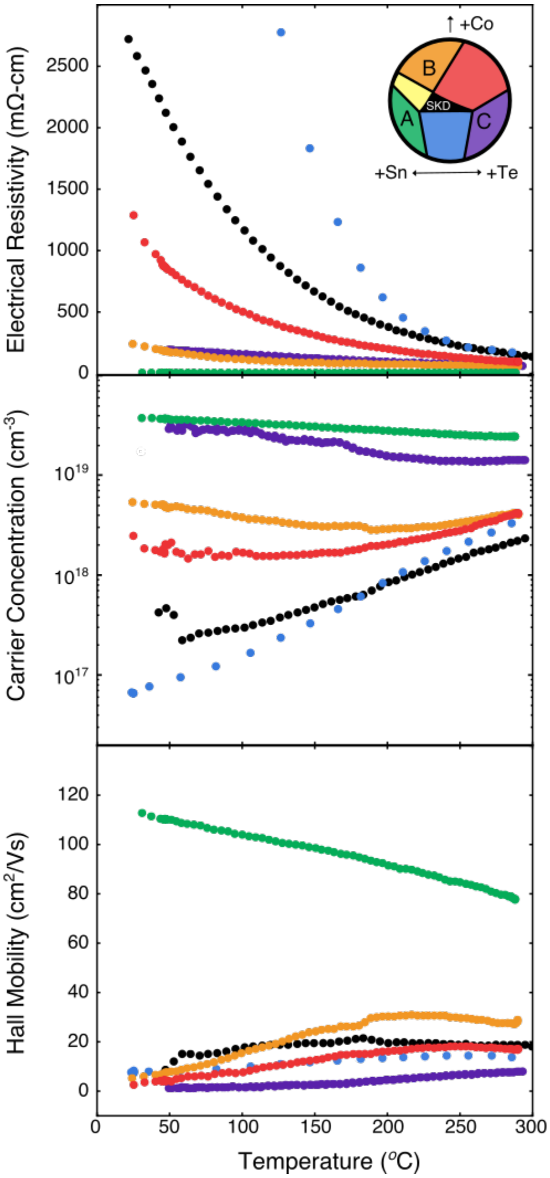

**Fig. 5** Resistivity, carrier concentration, and mobility data versus temperature. Transport data is color-coded with the regions observed in the inset in the resistivity plot. Note this is the same composition space as observed in the inset from Fig. 3.

also depend on the growth conditions. To further understand the experimentally observed variations in electronic properties and their dependence on the native defect chemistry as well as opportunities for extrinsic doping, we utilize first-principles defect calculations. In Eq. 1 (see Computational Methods), the dependence of defect formation energy ($\Delta H_{D,q}$) on growth conditions is captured through the chemical potentials ($\mu_i$) of the elements. The phase stability region of $Co_4Sn_6Te_6$ is defined by the bounds on $\mu_{Co}$, $\mu_{Sn}$, and $\mu_{Te}$. We begin by establishing the phase stability region of $Co_4Sn_6Te_6$ in the Co-Sn-Te ternary chemical potential space. The variations in the defect energetics across this phase stability region are then examined. Subsequently, we identify opportunities for extrinsic doping under specific chemical potential conditions.

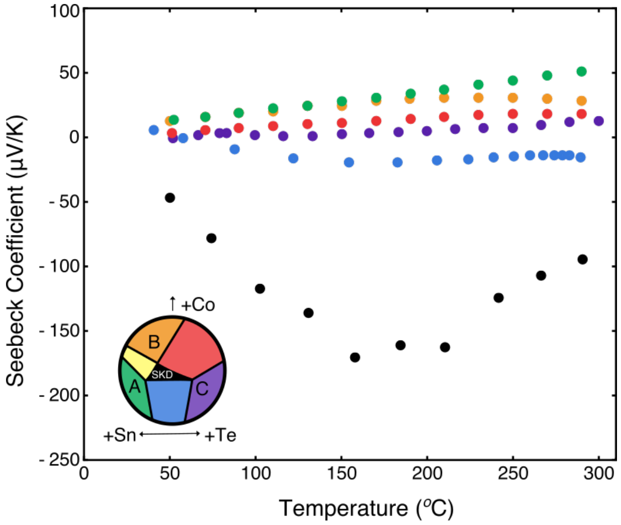

**Fig. 6** Seebeck data for samples around the single phase skutterudite region. We observe degenerate transport in the Sn-rich sample (shown in green). All other samples show intrinsic transport behavior. The inset serves as a guide to which compositional region the sample exists.

### 4.1 Phase Stability in Chemical Potential Space

To understand the variations in the defect formation energetics with growth conditions, we need to establish the phase stability of $Co_4Sn_6Te_6$ in the ternary Co-Sn-Te chemical potential space. Conventionally, the elemental chemical potential ($\mu_i$) is expressed as deviation from the reference elemental chemical potential. Mathematically, $\mu_i = \mu_i^0 + \Delta\mu_i$, where $\mu_i^0$ is the reference chemical potential and $\Delta\mu_i$ is the deviation from the reference potential. By definition, $\mu_i = \mu_i^0$, when the growth conditions correspond to equilibrium with the corresponding elemental phase under standard conditions such that such that $\Delta\mu_i = 0$. Therefore, $\Delta\mu_i = 0$ corresponds to the most $i$-rich growth conditions; the more negative the value of $\Delta\mu_i$ the $i$-poor are the growth conditions. The bounds on $\Delta\mu_i$ define the region of phase stability; the upper and lower bounds of $\Delta\mu_i$ are set by the region of phase stability.

In the absence of any competing phases, the compositional phase diagram is simply defined by its elemental end members. This can be mapped to the chemical potential space shown in Figure 7(a) as orthogonal planes. The planes are independent, as each phase only depends on a singular element. Single-phase regions span the facets shown in Figure 7(a). In this representation, no competing phases exist and thus the compositional phase diagram has a single three-phase region and three two-phase regions. The origin, where these three planes intersect, corresponds to the three-phase region in compositional space. Similarly, the lines formed by pairwise plane intersections correlate to the two-phase regions in compositional space.

When we consider the competing phases in the Co-Sn-Te chemical space, Figure 7(a) evolves significantly. Stable compounds exist as diagonal planes cutting through the elemental planes. These planes arise due to the relationship between Gibbs free energy (ΔG) and the available elemental chemical potentials ($\mu_i$). Here, we utilize calculations of $\Delta H_f$ as a low temperature proxy for ΔG as these results are obtained from first-principles ground-

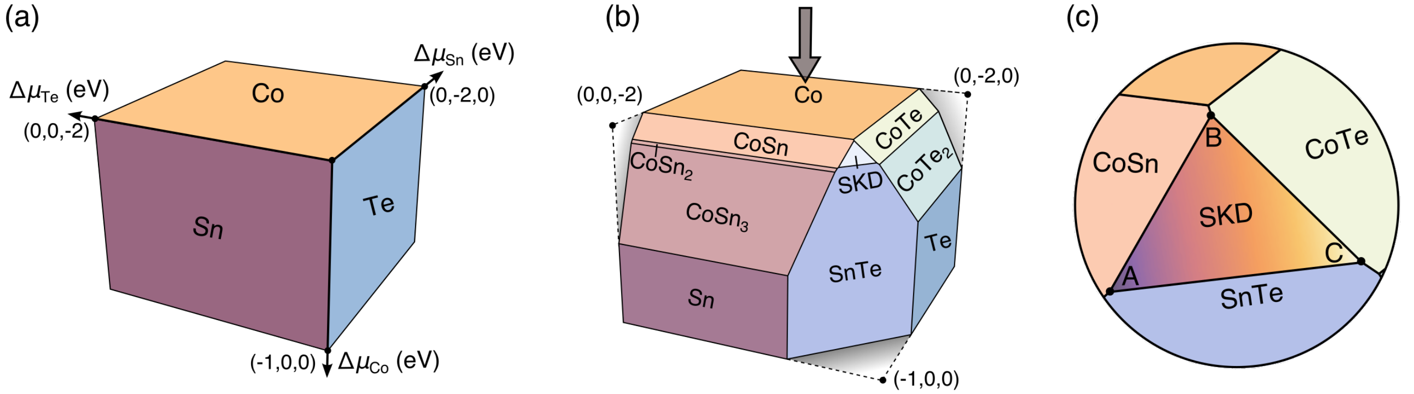

**Fig. 7** Chemical potential map for Co-Sn-Te: (a) Elemental chemical potential planes. Each plane corresponds to a pure elemental phase: Co (orange), Sn (purple), and Te(blue). The axes define the deviation from these reference planes. (b) Binary and ternary competing phases represent planes that intersect with the reference planes in (a). The skutterudite $Co_4Sn_6Te_6$ exists as a small facet (labeled SKD) indicating limted compositional stability, consistent with experimental findings. (c) Zoomed view of $Co_4Sn_6Te_6$ stability region. The invariant three-phase points are labeled A, B, and C. At A, SKD is in equilibrium with SnTe and CoSn; at B, with CoSn and CoTe; at C, with CoTe and SnTe. Coordinates for all three points can be found in supplemental (ES7).

state DFT calculations. Since all chemical potential values are negative in the region shown, $\Delta H_f$ of compounds in this region must also be negative. With the addition of each compound, the corresponding plane serves to form a new facet in Figure 7(b). These facets represent regions of single phase stability. For example, $Co_4Sn_6Te_6$'s plane is given by: $4\Delta\mu_{Co} + 6\Delta\mu_{Sn} + 6\Delta\mu_{Te} = -4.06\times16$ (where $\Delta H_f$ and $\Delta\mu_i$ values are determined via first-principles DFT calculations). Once again, two- and three-plane intersections (lines and points, respectively) translate to two- and three-phase regions in composition space. For example, point A in Figure 7(c) corresponds to the three-phase region (CoSn, SnTe, and $Co_4Sn_6Te_6$) in composition space, marked by A, in Figure 3 inset. We note that chemical potential space is often viewed in projection along one axis, however, Figure 7(b) presents an alternative view to highlight these planes.

Figure 7(c) presents a zoomed version of the phase stability region of $Co_4Sn_6Te_6$ in Figure 7(b). The three-phase points within the stability region of $Co_4Sn_6Te_6$ are marked as A, B, and C. The invariant points A, B, and C in Figure 7(c) can be mapped to the points marked A, B, and C in the composition space in Figure 3 inset. Due to possible inaccuracies in calculating the phase stability of $Co_4Sn_6Te_6$, we used the phase stability established from experiments (Figure 3) to slightly adjust the total energies ($\sim$ 30 meV/atom) obtained from DFT calculations. The computed phase stability diagram with the adjusted phase stability overlayed can be found in the supplementary information (ES7). Despite these adjustments, the conclusions about the predominant defects and therefore, the dopability remain qualitatively unchanged.

Changes in elemental chemical potentials directly alter the defect formation energies (Eq. 1), and therefore, the defect and carrier concentrations. Thus, the electronic properties can be expected to vary across the phase stability region of $Co_4Sn_6Te_6$. Experimentally, the synthesis of $Co_4Sn_6Te_6$ in the single-phase region can lead to samples that are not unique in their chemical potential conditions (Figure 7c). However, the three-phase points (A, B, C) correspond to unique growth conditions, thus, ensuring synthetic reproducibility. Probing these three-phase points using targeted synthesis is the core principle of phase boundary mapping. In the following sections, we examine how the defect energetics and dopability vary at the invariant three-phase points (A, B, and C).

### 4.2 Defect Diagrams

Defect energetics calculated from first-principles are typically presented in the form of defect diagrams *i.e.* defect formation energies $\left(\Delta H_{D,q}\right)$ as functions of Fermi energy ($E_F$), as shown in Figure 8. For a given material, one calculates the defect formation energies ($\Delta H$) of all defects of interest in all plausible charge states. The *x*-axis of the plot is the Fermi energy ($E_F$), which spans from the valence band maximum (VBM, conventionally set to 0) to the conduction band minimum (CBM). Since the only $E_F$-dependence in Equation 1 is linear, one can read the charge state off the plot according to the slope of each line. Defects with positive slopes act as donors while those with negative slopes are acceptors. For clarity, at any given $E_F$, only the charge state of the defect that has the lowest formation energy is shown; consequently, the defect plots in Figure 8 are the trace of the lowest-energy charge states. The charge transition levels (CTLs) are the points at which the energetically-favorable charge state changes. For instance, the 0/1- CTL of $Sn_{Te}$ is $\sim$60 meV from the valence band maximum. A defect is a shallow donor or acceptor if either there are no CTLs inside the band gap or the CTL is within a few $k_BT$ of the relevant band edge. Therefore, at room temperature and above, $Sn_{Te}$ behaves as a shallow acceptor.

The position of the equilibrium $E_F$, the corresponding defect concentrations, and the free carrier concentrations at a given temperature are calculated self-consistently by establishing the charge neutrality condition. For a given defect, all charge states are considered in solving the charge neutrality condition. The concentration of a defect $D$ at a given temperature and $E_F$ is de-

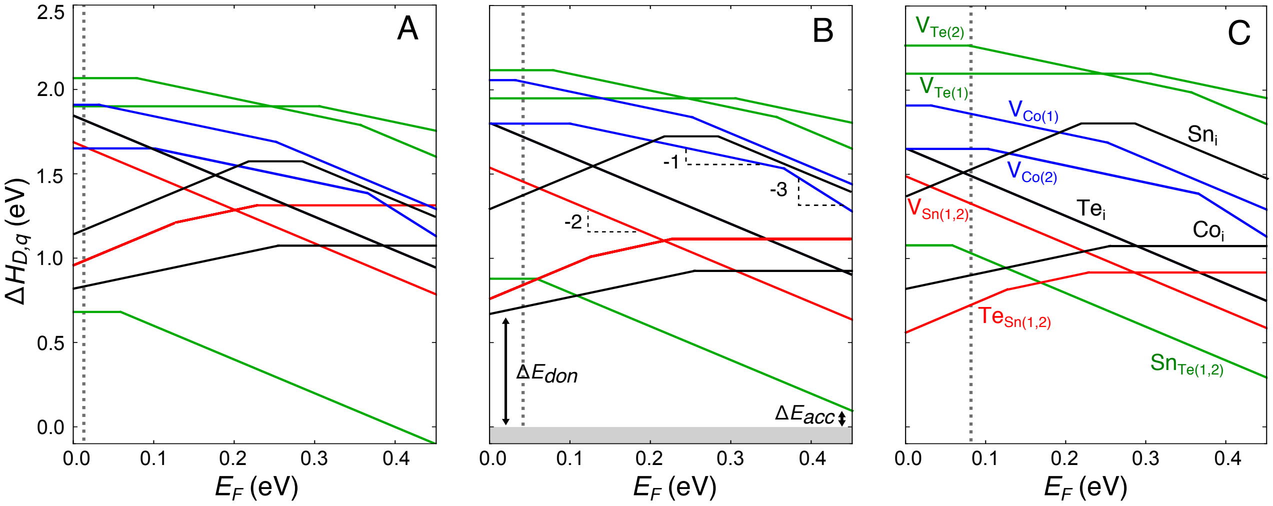

**Fig. 8** Defect formation energy ($\Delta H_{D,q}$) as a function of the Fermi energy ($E_F$) for $Co_4Sn_6Te_6$ under growth conditions corresponding to the chemical potentials at points A, B, and C shown in Figure 7 (c). $E_F$ is referenced to the valence band maximum and ranges from 0 eV to the calculated band gap (0.45 eV). The dominant defects include antisites $Te_{Sn}$ and $Sn_{Te}$ and Co interstitials. The subscripts (1) and (2) refer to different Wyckoff positions. The dopability window for donors ($\Delta E_{don}$) and acceptors ($\Delta E_{acc}$) are marked for growth conditions corresponding to the point B. Vertical dotted lines represent the equilibrium Fermi energy established by charge neutrality at T = 873 K.

termined from Bolztmann statistics:

$$[D] = N_s exp\left(-\frac{\Delta H_{D,q}}{k_B T}\right) \tag{2}$$

where $[D]$ is the defect concentration, $N_s$ is the concentration of possible lattice sites where the defect $D$ can be formed, $k_B$ the Boltzmann constant, and T the temperature. Carrier concentrations are determined by using the parabolic band approximations for both band edges. Effective masses used in the calculation of carrier concentrations are obtained from DFT electronic structure obtained on a dense k-point grid. Calculated conduction and valence band effective masses for $Co_4Sn_6Te_6$ are 4.514 $m_e$ and 0.17 $m_e$, respectively, where $m_e$ is the mass of an electron. In the following section, we examine the defect energetics at the invariant three-phase points (A, B, and C) and establish the equilibrium $E_F$ in each of those cases.

### 4.3 Defect Energetics and Equilibrium Fermi Energy

The calculated formation energetics of native defects in $Co_4Sn_6Te_6$ at the three invariant points (A, B, and C in Figure 7) are presented in Figure 8. At point A, corresponding to growth under relatively Sn-rich conditions, the predominant defect is the antisite $Sn_{Te}$, which is an acceptor defect. The equilibrium $E_F$ calculated from charge neutrality is 13 meV from the VBM (Figure 9); consequently, $Co_4Sn_6Te_6$ is $p$-type doped with free hole concentration of $\sim 2\times10^{18}$ $cm^{-3}$ at 873K (sample pressing temperature). The predicted high hole concentration is consistent with the experimental observation of degenerate transport in samples grown under Sn-rich conditions. However, at a pressing temperature of 673K, the predicted free hole concentrations drops to $7\times10^{17}$ $cm^{-3}$. The highest hole concentrations from self doping is obtained under Sn-rich conditions *i.e.* near point A. Therefore, if one is strictly limited to self-doping, Sn-rich conditions are required to yield sufficiently high hole concentrations. While beneficial for $p$-type doping, the acceptor $Sn_{Te}$ limits extrinsic $n$-type doping (see Section 4.4).

Using charge neutrality, the equilibrium $E_F$ can be determined at any point in the phase stability region of $Co_4Sn_6Te_6$. Figure 9 shows the equilibrium $E_F$ as a heatmap within the phase stability region projected along the Co chemical potential axis (projection direction indicated by arrow in Fig. 7). At point B, which cor-

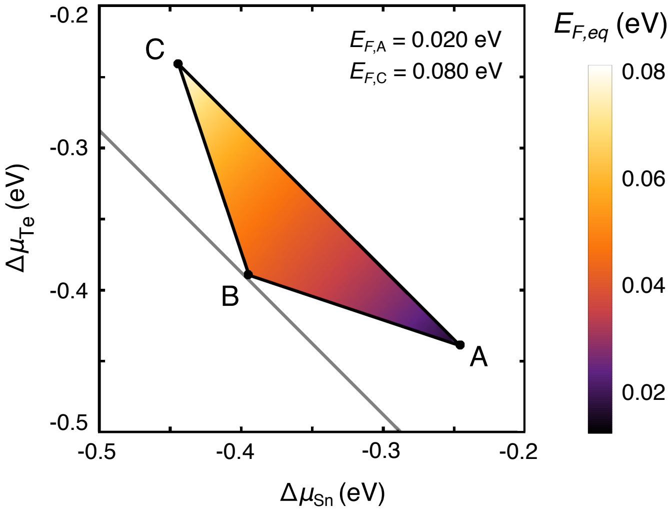

**Fig. 9** Equilibrium Fermi energy ($E_{F,eq}$) in the phase stability region of $Co_4Sn_6Te_6$, which is shown as a projection along the $\Delta\mu_{Co}$ axis (projection direction indicated by arrow in Figure 7(b)). $E_{F,eq}$ is referenced to the valence band maximum. Points A, B, and C are the three-phase points shown in Figure 7(c). The equilibrium $E_F$ lies below the mid-gap; $Co_4Sn_6Te_6$ ranges between natively $p$-type and $n$-type doped in the singe-phase region and the three-phase points.

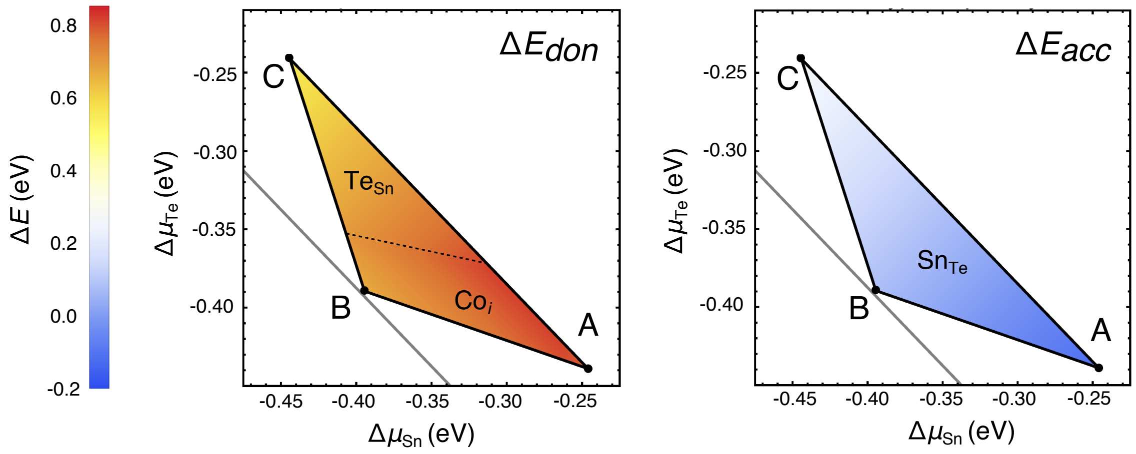

**Fig. 10** Donor ($\Delta E_{don}$) and acceptor ($\Delta E_{acc}$) dopability windows in the phase stability region calculated from the defect diagrams. The dopability windows at A, B, and C can be directly inferred from the defects diagrams in Figure 8. The predominant defects that set the dopability windows are labelled in the relevant regions of the phase stability; $\Delta E_{don}$ is set by $Te_{Sn}$ and $Co_i$ while $\Delta E_{acc}$ is determined solely by $Sn_{Te}$. A large dopability window indicates a higher potential for extrinsic doping. Given the large $\Delta E_{don}$ near A, the potential for extrinsic $p$-type doping is higher under Sn-rich growth conditions. The small or negative $\Delta E_{acc}$ means extrinsic $n$-type doping of $Co_4Sn_6Te_6$ is challenging under any growth conditions.

responds to growth under Co-rich conditions, antisites $Sn_{Te}$ (acceptor) and $Te_{Sn}$ (donor) and Co interstitials are the relevant low formation energy defects. The formation of Co interstitials is energetically favorable because of the Co-rich conditions at point B. In $Co_4Sn_6Te_6$, Co interstitial act as a donor, which is the expected behavior of cation interstitials. In contrast, Co interstitial in $CoSb_3$ was found to be an acceptor defect[54] due to the unique distortions of the $Sb_4$ rings that are absent in $Co_4Sn_6Te_6$. We also considered Sn and Te interstitials but their formation is found to be energetically unfavorable.

From the different growth conditions compared to point A (Sn-rich), the equilibrium $E_F$ is ~50 meV from the VBM and $Co_4Sn_6Te_6$ is self-doped $n$-type with electron concentration of $9\times10^{17}$ cm$^{-3}$ at 873K where the differences arise from the variable effective masses. Similarly, at point C, $Sn_{Te}$, $Te_{Sn}$, and $Co_i$ are the relevant low formation energy defects. Given the relatively Te-rich conditions at C, the antisite $Te_{Sn}$ has lower formation energy compared to points A and B. The equilibrium $E_F$ at 873K is roughly 80 meV from the VBM (Figure 9), again resulting in a self-doped $n$-type material with electron concentration of $6\times10^{18}$ cm$^{-3}$. The range of calculated carrier concentrations across the single-phase region is consistent with our experimental findings in samples having bipolar conduction. Therefore, within the phase stability region of $Co_4Sn_6Te_6$ the equilibrium $E_F$ ranges from 13 meV (at A) to 80 meV (at c) from the VBM. The corresponding carrier concentrations range from $9\times10^{17}$ e$^-$ cm$^{-3}$ to $2\times10^{18}$ h$^+$ cm$^{-3}$ at 873 K.

### 4.4 Assessing Dopability

Based on the formation energetics of the native defects, we now assess the potential for extrinsic $p$- and $n$-type doping of $Co_4Sn_6Te_6$ under various growth conditions *i.e.* different elemental chemical potentials in the phase stability region. When an extrinsic dopant is introduced, there will be charge compensation if an oppositely charged native defect intersects with the dopant defect. For instance, the dopability window for extrinsic $p$-type doping is set by the energetic room provided by the lowest energy donor at the VBM. See for example, $\Delta E_{don}$ labelled in Figure 8(b) where the lowest energy donor is Co interstitial and the trace of Co interstitial defect at the VBM is 0.67 eV. Therefore, a suitable extrinsic acceptor dopant whose trace at the VBM is below 0.67 eV will not suffer from hole compensation due to the Co interstitials and will likely be an effective $p$-type dopant. Similarly, the intercept of the lowest energy native acceptor defect at the CBM sets the dopability window ($\Delta E_{acc}$) for $n$-type doping.

As the defect energetics vary significantly within the stability region, we calculate $\Delta E_{don}$ and $\Delta E_{acc}$ at all chemical potentials across the single-phase region (Figure 10). Larger the value of $\Delta E_{don}$, the higher the potential for introducing an effective $p$-type dopant. Similarly, the larger the value of $\Delta E_{acc}$, the higher the potential for extrinsic $n$-type doping. Note that the lowest energy donor that sets $\Delta E_{don}$ changes from Co interstitial to $Te_{Sn}$ as we move from Sn-rich and Co-rich to Te-rich conditions. The dopability window $\Delta E_{don}$ is fairly large across the entire single-phase region, with the largest window of ~0.8 eV present under Sn-rich growth conditions (point A). For extrinsic $p$-type doping, it is, therefore, most promising to dope under Sn-rich growth conditions. In contrast, the lowest energy acceptor is $Sn_{Te}$ across the entire single-phase region. The low energy of $Sn_{Te}$ limits $\Delta E_{acc}$ to small positive or negative values. Consequently, efficient extrinsic $n$-type doping is predicted to be challenging in $Co_4Sn_6Te_6$.

## 5 Conclusions

Achieving superior thermoelectric performance in $p$-type skutterudites has long been challenging. In this foundational study, we consider the properties of mixed-anion skutterudites with a focus on phase stability and associated electronic defects. As evidenced by the alloying study between $Co_4Sb_{12}$ and $Co_4Sn_6Te_6$, we established there is a strong driving force for partitioning into the respective skutterudite end-member phases. We conclude this is in part due to the anion framework not accommodating significant quantities of variable anions. The thermodynamic driving force to form SnTe, may be too much to overcome when trying to establish a new phase in this quaternary system. Inspired by prior reports of the $Co_4Sn_6Te_6$ electronic structure and inconclusive transport data, we established the ternary phase diagram, measured thermoelectric properties at the phase boundary invariant points, and conducted a study of the intrinsic defects. Phase boundary mapping established the presence of three invariant points that bound the single phase $Co_4Sn_6Te_6$ region. Two of these invariant points reveal highly compensated, intrinsic electronic behavior, while the Sn-rich third invariant point exhibits degenerate $p$-type behavior ($\sim 2\times 10^{19}$ $h^+$ $cm^{-3}$). In the latter case, high room temperature mobility ($>110$ $cm^2/V\cdot s$) was observed, which decayed to 80 $cm^2/V\cdot s$ by 300°C. To understand these results and the potential for extrinsic dopants, we turned to defect calculations. Our calculations revealed that $Sn_{Te}$, $Co_i$, and $Te_{Sn}$ are the most common defects, with $Sn_{Te}$ driving the degenerate behavior in Sn-rich conditions. The defect calculations further revealed that extrinsic $p$-type doping is unlikely to be limited by donor counter-defects whereas $n$-type doping may be quite difficult to achieve. As such, future work on controlling the electronic properties of $Co_4Sn_6Te_6$ through the introduction of a $p$-type dopant is promising.

## 6 Acknowledgments

This work was performed at the California Institute of Technology/Jet Propulsion Laboratory under contract with the National Aeronautics and Space Administration. This work was supported by the NASA Science Missions Directorate's Radioisotope Power Systems Thermoelectric Technology Development Project under Grant/Contract/Agreement No. NNX16AT18H. We also acknowledge support from the National Science Foundation (NSF) DMR grants 1729594 and 1555340. The research was performed using computational resources sponsored by the Department of Energy's Office of Energy Efficiency and Renewable Energy and located at the NREL. Use of the Advanced Photon Source at Argonne National Laboratory was supported by the U. S. Department of Energy, Office of Science, Office of Basic Energy Sciences, under Contract No. DE-AC02-06CH11357.

## References

1 G. J. Snyder and E. S. Toberer, *Nature Materials*, 2008, **7**, 105–114.

2 G. A. Lamberton, S. Bhattacharya, R. T. Littleton, M. A. Kaeser, R. H. Tedstrom, T. M. Tritt, J. Yang, G. S. Nolas and R. T. Littleton IV, *Applied Physics Letters*, 2002, **80**, 1855–182101.

3 Y. Tang, R. Hanus, S. W. Chen and G. J. Snyder, *Nature Communications*, 2015, **6**, 1–7.

4 G. S. Nolas, M. Kaeser, R. T. Littleton IV and T. M. Tritt, *Applied Physics Letters*, 2000, **771**, 1855–182101.

5 L. Zhang, A. Grytsiv, P. Rogl, E. Bauer and M. Zehetbauer, *J. Phys. D: Appl. Phys.*, 2009, **42**, 225405.

6 J. G. Snyder, Y. Tang, C. M. Crawford and E. S. Toberer, *Materials Aspect of Thermoelectricity*, CRC Press, 1st edn, 2016, ch. 19.

7 G. S. Nolas, G. Fowler and J. Yang, *Journal of Applied Physics*, 2006, **100**, 043705.

8 T. Caillat, A. Borshchevsky, J.-P. Fleurial and . A. Borshchevsky, *Applied Physics Letters*, 1996, **80**, 1013–1855.

9 B. C. Sales, D. Mandrus and R. K. Williams, *Science*, 1996, **272**, 1325–1328.

10 G. S. Nolas, D. T. Morelli and T. M. Tritt, *Annual Review of Materials Science*, 1999, **29**, 89–116.

11 C. Uher, *Semiconductors and Semimetals*, Elsevier Ltd., 69th edn, 2001, ch. 5, pp. 139–253.

12 B. C. Sales, D. Mandrus, B. C. Chakoumakos, V. Keppens and J. R. Thompson, *Physical Review B*, 1997, **56**, 15081–15089.

13 E. S. Toberer, A. Zevalkink and G. J. Snyder, *Journal of Materials Chemistry*, 2011, **21**, 15843.

14 M. Puyet, B. Lenoir, A. Dauscher, M. Dehmas, C. Stiewe and E. Müller, *Journal of Applied Physics*, 2004, **95**, 4852.

15 K.-H. Park, I.-H. Kim, S.-M. Choi, W.-S. Seo, D.-I. Cheong and H. Kang.

16 J. W. Sharp, E. C. Jones, R. K. Williams, P. M. Martin and B. C. Sales, *Journal of Applied Physics*, 1995, **78**, 1013–4442.

17 R. C. Mallik, R. Anbalagan, K. K. Raut, A. Bali, E. Royanian, E. Bauer, G. Rogl and P. Rogl, *J. Phys.: Condens. Matter*, 2013, **25**, 105701–10.

18 D. Volja, B. Kozinsky, A. Li, D. Wee, N. Marzari and M. Fornari, *Physical Review B*, 2012, **85**, 245211.

19 K. Momma and F. Izumi, *Journal of Applied Crystallography*, 2008, **41**, 653–658.

20 R. Korenstein, S. Soled, A. Wold and G. Collin, *Inorganic Chemistry*, 1977, **16**, 2344–2346.

21 Y. Nagamoto, K. Tanaka and T. Koyanagi, XVI ICT '97. Proceedings ICT'97. 16th International Conference on Thermoelectrics (Cat. No.97TH8291), 1997, pp. 330–333.

22 F. Laufek, J. Návrátil and V. Goliáš, *Powder Diffraction*, 2008, **23**, 15–19.

23 M. Partik and H. D. Lutz, *Physics and Chemistry of Minerals*, 1999, **27**, 41–46.

24 P. Vaqueiro, G. G. Sobany, A. V. Powell and K. S. Knight, *Journal of Solid State Chemistry*, 2006, **179**, 2047–2053.

25 L. Bertini and S. Cenedese, *Phys. stat. sol. (RRL)*, 2007, **1**, 244–246.

26 A. Kaltzoglou, A. V. Powell, K. S. Knight and P. Vaqueiro, *Journal of Solid State Chemistry*, 2013, **198**, 525–531.

27 G. S. Nolas, J. Yang and R. W. Ertenberg, *Physical Review B*, 2003, **68**, 193206.

28 J. Navrátil, T. Plecháček, L. Beneš, Č. Drašar and F. Laufek, *Journal of Electronic Materials*, 2010, **39**, 1880–1884.

29 J. Navrátil, T. Plecháček, L. Beneš and M. Vlček, *Chalcogenide Letters*, 2004, **1**, 73–76.

30 P. Vaqueiro and G. G. Sobany, *Mater. Res. Soc. Symp. Proc.*, 2008, **1044**, 1044–U05–08.

31 P. Vaqueiro, G. G. Sobany and M. Stindl, *Journal of Solid State*

*Chemistry*, 2008, **181**, 768–776.

32 F. Laufek, J. Navrátil, J. Plášil, T. Plecháček and Č. Drašar, *Journal of Alloys and Compounds*, 2009, **479**, 102–106.

33 H. Chi, H. Kim, J. C. Thomas, X. Su, S. Stackhouse, M. Kaviany, A. Van Der Ven, X. Tang and C. Uher, *Physical Review B - Condensed Matter and Materials Physics*, 2012, **86**, 1–7.

34 K. Wei, Y. Dong, P. Puneet, T. M. Tritt and G. S. Nolas, *Journal of Alloys and Compounds*, 2014, **614**, 330–333.

35 A. Zevalkink, K. Star, U. Aydemir, G. J. Snyder, J.-P. Fleurial, S. Bux, T. Vo and P. von Allmen, *Journal of Applied Physics*, 2015, **118**, 035107.

36 Z. X. Liang Y, Fang B and L. M. M, *17th IUMRS International Conference in Asia*, 2016.

37 S. Bang, D. Wee, A. Li, M. Fornari and B. Kozinsky, *Journal of Applied Physics*, 2016, **119**, 205102.

38 J. Navrátil, T. Plechá, Č. Drašar, M. Vl, L. Beneš and F. Laufek, 6th European Conference on Thermoelectrics, 2009, pp. 1–5.

39 Y. Dong, K. Wei and G. S. Nolas, *Physical Review B - Condensed Matter and Materials Physics*, 2013, **87**, 1–5.

40 S. Ohno, U. Aydemir, M. Amsler, J. H. Pöhls, S. Chanakian, A. Zevalkink, M. A. White, S. K. Bux, C. Wolverton and G. J. Snyder, *Advanced Functional Materials*, 2017, **27**, 1–10.

41 S. Ohno, K. Imasato, S. Anand, H. Tamaki, S. D. Kang, P. Gorai, H. K. Sato, E. S. Toberer, T. Kanno and G. J. Snyder, *Joule*, 2017, 1–14.

42 S.-m. Tseng, S.-w. Chen, J.-s. Chang, Y. Tang and G. J. Snyder, *Metallurgical and Materials Transactions E*, 2015, **2**, 236–249.

43 Y. Tang, S. wen Chen and G. J. Snyder, *Journal of Materiomics*, 2015, **1**, 75–84.

44 Y. Qiu, L. Xi, X. Shi, P. Qiu, W. Zhang, L. Chen, J. R. Salvador, J. Y. Cho, J. Yang, Y. C. Chien, S. W. Chen, Y. Tang and G. J. Snyder, *Advanced Functional Materials*, 2013, **23**, 3194–3203.

45 J. Perl, J. Shin, J. Schümann, B. Faddegon and H. Paganetti, *Medical Physics*, 2012, **39**, 6818–6837.

46 K. A. Borup, E. S. Toberer, L. D. Zoltan, G. Nakatsukasa, M. Errico, J.-P. Fleurial, B. B. Iversen and G. J. Snyder, *Rev. Sci. Instrum.*, 2012, **83**, 123902–105119.

47 S. Lany and A. Zunger, *Phys. Rev. B*, 2008, **78**, 235104.

48 A. Goyal, P. Gorai, H. Peng, S. Lany and V. S. Stevanović, *Comp. Mat. Sci.*, 2016, **130**, 1.

49 J. P. Perdew, K. Burke and M. Ernzerhof, *Phys. Rev. Lett.*, 1996, **77**, 3865.

50 G. Kresse and J. Furthmüller, *Phys. Rev. B*, 1996, **54**, 11169.

51 S. L. Dudarev, G. A. Botton, S. Y. Savrasov, C. J. Humphreys and A. P. Sutton, *Phys. Rev. B*, 1998, **57**, 1505.

52 P. Gorai, B. R. Ortiz, E. S. Toberer and V. Stevanović, *J. Mater. Chem. A*, 2018, **6**, 13806.

53 B. R. Ortiz, C. M. Crawford, R. W. McKinney, P. A. Parilla and E. S. Toberer, *J. Mater. Chem. A*, 2016, **4**, 8444–8450.

54 G. Li, S. Bajaj, U. Aydemir, S. Hao, H. Xiao, W. A. Goddard, P. Zhai, Q. Zhang and G. J. Snyder, *Chemistry of Materials*, 2016, **28**, 2172.

# Table of Contents Entry

Investigating Phase Space of $Co_4Sn_6Te_6$ Skutterudite

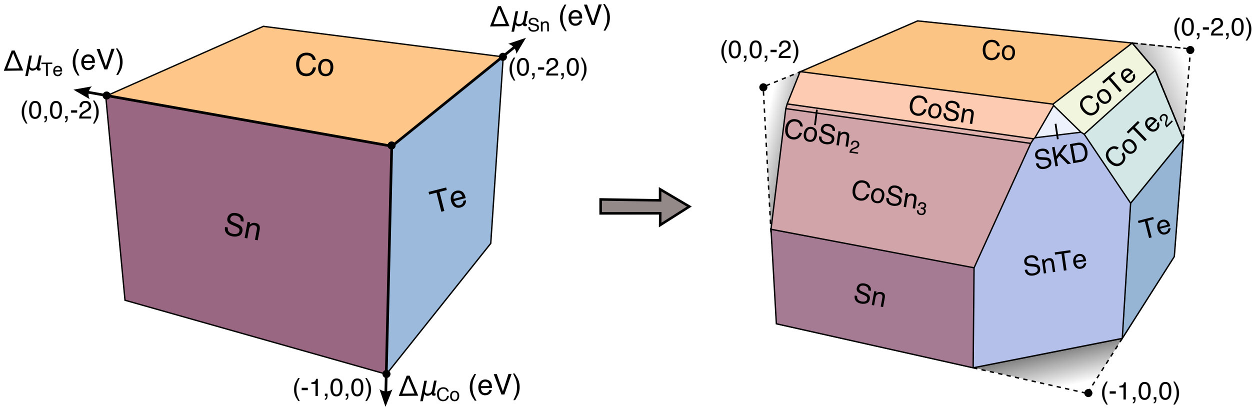

Experimental and computational investigation of the phase stability and thermoelectric properties of the $Co_4Sn_6Te_6$ skutterudite.